LAWRENCE
LIVERMORE
NATIONAL
LABORATORY

LLNL-JRNL-640914

Nanoindentation behavior of nanotwinned Cu: influence of indenter angle on hardness, strain rate sensitivity, and activation volume

I. C. Choi, Y. J. Kim, Y. M. Wang, U. Ramamurty, J. Jang

July 12, 2013

Acta Materialia

Disclaimer

Nanoindentation behavior of nanotwinned Cu: Influences of indenter angle on hardness, strain rate sensitivity, and activation volume

In-Chul Choi,[1] Yong-Jae Kim,[1] Y. Morris Wang,[2] Upadrasta Ramamurty,[3] Jae-il Jang[1,*]

[1]Division of Materials Science and Engineering, Hanyang University, Seoul 133-791, Korea

[2]Physical and Life Sciences Directorate, Lawrence Livermore National Laboratory, Livermore, CA 94550, USA

[3]Department of Materials Engineering, Indian Institute of Science, Bangalore 560012, India

*Corresponding author: jijang@hanyang.ac.kr

ABSTRACT

The influence of strain on the mechanical properties and deformation kinetic parameters of nanotwinned (nt) copper is investigated by a series of nanoindentation experiments, which were performed by employing sharp indenters with five varying centerline-to-face angles (ψ). Comparison experiments were also conducted on (110) single crystalline Cu. Experimental results indicate that unlike coarse-grained materials, nt-Cu is prone to plastic flow softening with large material pile-up around the indentation impression at high levels of strains. Localized detwinning becomes more significant with the decreasing ψ, concomitant with reduced strain rate sensitivity (m) and enhanced activation volume (V^*). The m of nt-Cu is found to depend sensitively on the ψ with a variation of more than a factor of 3, whereas the V^* exhibits a much less sensitive trend. We discuss the validation of the experimental techniques and implications of various deformation kinetic parameters on the underlying deformation mechanisms of nt-Cu.

Keywords: Nanotwinned metals; Nanoindentation; Hardness; Strain rate sensitivity; Activation volume.

1. Introduction

Nanocrystalline (nc) metals and alloys (with grain size d < 100 nm) exhibit ultrahigh strength, excellent wear resistance, and possibly superplastic formability at low temperatures and/or high strain rates [1]. This far superior mechanical behavior, in comparison to conventional single crystalline and coarse-grained (cg) metals, is a result of the high concentration of incoherent grain boundaries (GBs) that obstruct dislocation motion. However, the enhanced strength comes at the expense of reduced ductility [2,3]. Compared with ordinary GBs, coherent twin boundaries (TBs) usually exhibit much higher thermal and mechanical stability. Recent studies have shown that the controlled introduction of nanoscale twin boundaries (TBs), with a spacing λ < 100 nm, into the microstructure causes significant strengthening (that is quantitatively identical to that from GBs [2]) while preserving acceptable levels of ductility [2,4]. These nanotwinned (nt) metals with nanoscale growth twins also exhibit thermal stability [5] vis-à-vis incoherent GBs and electrical conductivity [6].

The strain-rate sensitivity (SRS, m) and the activation volume (V^*) are useful quantitative indicators of the predominant mechanism of a stress-assisted, thermally-activated plastic deformation [7-9]. Recent studies have revealed that, similar to nc metals, nt metals also exhibit an enhanced SRS and reduced V^* in comparison with their single crystal and cg counterparts. This elevated SRS may help in delaying the necking during tensile deformation and can contribute to ductility. Table 1 provides a summary of the experimental data available in the literature on the m and V^* of nt-Cu, a widely examined nt-metal, with various λ [1,7,10-12]. Note that the single crystal and cg-Cu have m values of 0.006 and 0.004-0.007, respectively, and their V^* is ~$1000b^3$ where b is the Burger's vector [13,14]. From Table 1, it is seen that unless the grain size effect is considered, m scales inversely with the average λ, which is close to the effects

of grain size *d* in nc-Cu in previous literature [11,15].

Typically, nanoindentation is employed for evaluating the mechanical properties of nc-/nt-metals [11,16-20]. This is due to the advantages that this technique offers such as simple procedure and the requirement of only a small volume of material. The latter enables the collection of statistically significant data even on the nc-/nt-metals, whose available sample size is still limited. In particular, nanoindentation is extensively utilized for examining the SRS behavior of these materials as indentation strain rates can be varied over four orders of magnitude systematically [17]. Additionally, nanoindentation experiments allow one to explore the deformation behavior of nanostructured materials in a strain range that is well beyond that achievable from tensile tests. These merits made it possible to systematically investigate many factors affecting SRS of nt metals through nanoindentation experiments. For example, recently, Ye et al. [11] analyzed the effects of twin-orientation (to loading direction) and surface polishing on *m* of nt-Cu through nanoindentation experiments. It was found that indentation on the plan-view surface (having TBs perpendicular to loading direction) produces higher *m* than that on the cross-sectional surface (with TBs parallel to loading direction) and that the value of *m* obtained on the mechanically-polished surface (having larger initial dislocation density) is higher than that from the as-deposited surface [11].

Despite above advantages, however, microstructural instability is often observed during the nanoindentation of nc or nt materials [7,10]. The problem is further compounded by another important but unresolved issue related to *m*. It is known that the value of *m* in metallic materials depends strongly on the plastic strain level, which could be even more so for nc or nt materials. However, this issue has not yet been examined critically, mainly because of the difficulty in varying strains during nanoindentation tests wherein a three-sided pyramidal indenter (such as

Berkovich indenter) is routinely employed. Note that the deformation fields underneath a given sharp indenter are affine from the continuum plasticity point of view, due to the geometrical self-similarity of the tip. It is possible to overcome this issue by employing different indenters. The sharpness of the triangular pyramidal indenter as characterized by its centerline-to-face angle, ψ, can be varied. Generally, sharper indenters induce larger strains in the material due to the larger volume of material that is displaced [21-24]. Thus, indentations made with different ψ lead to different level of strains, allowing a systematic evaluation of the strain effects.

With all the above issues in mind, we explore here the influence of the strains on the plastic deformation, strain-rate sensitivity, and activation volume of nt-Cu through a series of nanoindentation experiments using five different indenters having various ψ. In addition, the tests under the identical condition were carried out on (110) single crystal Cu for comparison purposes. The results reveal that the nature of plastic flow in nt-Cu is significantly affected by the level of applied strain, which is discussed in terms of changes in rate-sensitive deformation mechanism and microstructures underneath the indenter.

2. Experimental

A ~170 μm-thick Nt-Cu foil was prepared by layer-by-layer deposition of high-purity (> 99.99%) Cu onto a (100) silicon wafer through d.c. magnetron sputtering. Details of this procedure are described in [12]. The grains are columnar in nature and their diameter is of the order of 0.5-3.0 μm with a twin lamella spacing ranging between 40 and 80 nm. For comparison purposes, the (110) facet of single crystalline (sc) Cu was also examined. The sample surfaces were initially ground with fine SiC papers and gently polished with a microcloth using 0.3 μm

alumina. The sample was given a final electrolytic-polishing for removing any possible surface damage that is induced during prior mechanical polishing.

Nanoindentation experiments were performed at room temperature using Nanoindenter-XP (formerly MTS; now Agilent, Oak Ridge, TN). Five different three-sided pyramidal indenters with centerline-to-face angles, ψ, of 35.3° (cube-corner), 50°, 65.3° (Berkovich), 75°, and 85° were employed. During the tests, the specimen was loaded to a fixed peak load, P_{max}= 100 mN with indentation strain rates, $\dot{\varepsilon}_i$ (= h^{-1}(dh/dt and is equal to half the loading rate P^{-1}(dP/dt) [25]) of 0.01, 0.025, 0.05, and 0.125 /s. For each combination, more than 30 tests were conducted so as to obtain statistically significant hardness values. Thermal drift was maintained below 0.1 nm/s in all experiments. The hardness impressions were imaged using a field-emission scanning electron microscopy (FE SEM), JSM-6330F (JEOL Ltd., Tokyo, Japan). The topolography of the indented surface was measured with an XE-100 atomic force microscope (AFM; Park Systems, Suwon, Korea). The indentation direction for nt-Cu is vertical to the growth plane.

In order to observe microstructural changes – if any – that occur due to the deformation right underneath the indenter, specimens for transmission electron microscopy (TEM) were prepared through Focused Ion Beam (FIB) milling with Nova 200 NanoLab (FEI Co, Hillsboro, OR). At around the vertex of the indented impression, a thin slice is milled and lifted. To minimize the possibility of beam-induced heating, the Ga ion beam intensity and acceleration voltage were kept as low as 10 pA and 30 kV, respectively. TEM was performed in the scanning mode (STEM) as well as high resolution (HR) mode with the aid of a Tecnai F20 (FEI Co, Hillsboro, OR).

3. Results

3.1 Load-displacement curves and plasticity

Figure 1a shows the representative load-displacement (P-h) plots obtained on nt-Cu with different indenters and at different $\dot{\varepsilon}_i$ with P_{max} = 100 mN. Corresponding plots obtained on sc-Cu are displayed in Fig. 1b. For clarity, the top segments of the curves for ψ = 85° are magnified in the inset. For both nt-Cu and sc-Cu, the displacement at the peak load, h_{max}, increases with decreasing ψ. Importantly, significant rate-dependency was observed in nt-Cu, with h_{max} decreasing as $\dot{\varepsilon}_i$ is increased for any given value of ψ. However, such rate-dependency is clearly less pronounced for sc-Cu.

The ratio of the residual displacement after complete unloading, h_f, to h_{max} is an indicator of the relative portion of the plastic deformation in the total elasto-plastic deformation that occurs during indentation. The variations in h_f/h_{max} with $\dot{\varepsilon}_i$ are summarized in Fig. 2, which indicate to the following: For a given $\dot{\varepsilon}_i$ - ψ combination, the h_f/h_{max} value obtained on nt-Cu is much lower than that measured on sc-Cu, which implies that plasticity in the former is less pronounced than the latter. In both the cases, a higher h_f/h_{max} is obtained with a sharper indenter and for faster indentation.

3.2 Hardness variation

From the P-h curves, values of nanoindentation hardness, $H_{O\text{-}P}$, were estimated according to the Oliver-Pharr (O-P) method [26]. The area function for each indenter (which is essential to calculate the hardness) was determined through preliminary indentation tests made on fused quartz. Variations of $H_{O\text{-}P}$ with ψ for both nt- and sc-Cu are displayed in Fig. 3. The hardness of nt-Cu obtained with the Berkovich indenter (ψ = 65.3°), 2.44±0.038 GPa, is in a good agreement

with literature data [5,7,11,27,28], while no comparable data for other indenter angles are currently available in the literature. The hardness of sc-Cu obtained from Berkovich indentations, 0.541±0.004 GPa, is slightly lower than that reported by Vlassak and Nix [29], which may be due to either indentation size effect (h_{max} is ~1000 nm in [29] whereas it is ~2000 nm in this study) or different surface preparation methods (mechanical polishing in [29] and electrolytic polishing in this study).

In Fig. 3, two trends are obvious from the results on nt-Cu. First, as expected from the *P*-*h* curves in Fig. 1a, the $H_{O\text{-}P}$ for each indenter is unambiguously rate-sensitive and increases with increasing $\dot{\varepsilon}_i$. In contrast, $H_{O\text{-}P}$ is insensitive to $\dot{\varepsilon}_i$ in the case of sc-Cu. Second, the $H_{O\text{-}P}$ increases with decreasing ψ, except for $\psi = 35.3°$ whose $H_{O\text{-}P}$ value lower than that for $\psi = 50°$. For sc-Cu, $H_{O\text{-}P}$ decreases linearly with $\dot{\varepsilon}_i$ throughout the entire range of ψ investigated. This is the expected trend in metals and alloys that exhibit strain hardening.

It is possible that the trends for nt-Cu are conceivably an artifact arising from the uncertainty about the applicability of the Oliver-Pharr method [26] to various indenter angles. For example, the correlation constant β (that relates stiffness S to area A and thus important for determining the area function and thus the $H_{O\text{-}P}$) is known only for the commonly-used Berkovich indenter (as a constant of 1.034 [30]), and the dependency of the β value on the indenter angle is still unclear although some efforts have been made [31]. This may result in miscalculations of the hardness data for other indenters adopted in this study. To examine this critically, we estimated the Mayer's hardness, H_M, by measuring the impression size (or contact area) A directly from a large number of SEM images for $\psi = 35.3$, 50, 65.3, and 75° (see Fig. 4). Note that the contact area for $\psi = 85°$ could not be measured because of the difficulty in identifying the true edge of the impression, which is a result of the relatively shallow indentation

depth in this case. Values of A are listed in Table 2. H_M is then estimated using the following relation:

$$H_M = h_{max} / A = 4h_{max} /(3\sqrt{3}a^2) \quad (1)$$

where a is the averaged length measured from the center of the triangular impression to the corner. H_M and $H_{O\text{-}P}$ are compared in Fig. 5 for both nt-Cu and sc-Cu. As expected, H_M and $H_{O\text{-}P}$ of sc-Cu are identical. In contrast, H_M is lower than $H_{O\text{-}P}$ in the case of nt-Cu. The trends in H_M and $H_{O\text{-}P}$ with ψ are somewhat similar; particularly, H_M of nt-Cu for $\psi = 35.3°$ is indeed lower than that for $\psi = 50°$ (just as $H_{O\text{-}P}$), supporting that the trend of nt-Cu seen in Fig. 3 is not an artifact. While H_M and $H_{O\text{-}P}$ are almost identical for sc-Cu, H_M of nt-Cu is slightly lower than its $H_{O\text{-}P}$. This may be because the material pile-up around indentation (that is pronounced only in nt-Cu, as discussed below), which is not taken into consideration in the Oliver-Pharr method and thus can induce an overestimated $H_{O\text{-}P}$ [32,33].

3.3 Indentation morphology

Representative SEM micrographs of the indents displayed in Fig. 4 show no cracking in all the indentations, suggesting fully plastic flow in nt- and sc-Cu. In the latter case, no pile-up could be seen. In contrast, the pile-up behavior in nt-Cu is was found to be sensitive to ψ. For $\psi \geq 65.3°$, there was little pile-up. In contrast, significant pile-up is seen for $\psi \leq 50°$ and the pile-up becomes pronounced with decreasing ψ. For sharper indenters (especially, $\psi = 35.3°$), the morphology of the pile-up is that of shear off steps indicating to inhomogeneous or localized plastic flow. These features are similar to those reported in nc alloys as well as metallic glasses [34]. Trelewicz and Schuh [17], who investigated Ni-W alloy as a function of the grain size, d, observed that in nc-metals having very small d (d < ~10 nm), the pile-up becomes

inhomogeneous (i.e., plastic flow is shear band mediated just as in metallic glasses), activation volume increases, and SRS decreases, which is similar to what observed here for small ψ.

Figure 6 shows the representative AFM images of selected indents and line scans across them in nc- and sc-Cu samples. The inhomogeneous nature of the pile-up in nt-Cu is evident with steps on the line scan of nt-Cu (Fig. 6a). Even from the same cube-corner indenter, the pile-up behavior is almost negligible for sc-Cu (Fig. 6b). From the AFM surface profile data, the ratio of pile-up height, $h_{\text{pile-up}}$, to $h_{\max}$ for each indenter was measured and the results are summarized in Fig. 7. This ratio is negligible for sc-Cu and is almost ψ-independent. In contrast, $h_{\text{pile-up}}/h_{\max}$ ratio is significant in the case of nt-Cu.

4. Discussion

4.1 Stress-strain responses

We convert H vs. ψ data into stress vs. strain, which would give us insights into the plastic flow behavior of nt-Cu, as following. For converting H into flow stress, $\sigma_{f,i}$, we employ the well-known empirical relationship originally suggested by Tabor [35];

$$H = C_\theta \cdot \sigma_{f,i} \tag{2}$$

where C_θ is the constraint factor, which is typically in the range 2.6–3.0 [35,36] for metallic materials in the fully plastic regime of indentation. However, the validation of the constraint factor to nc- or nt-materials has recently become questionable due to the significantly different strain hardening behavior of these materials and uncertainties arisen from tensile results [37]. It is thus important to address this issue for nt-Cu tested here. Furthermore, C_θ would be a strong function of ψ in the elasto-plastic regime [38]. In this regime, Johnson [38] estimated C_θ as

$$C_\theta = \frac{2}{3}\left[1 + \ln\left(\frac{E}{\sigma_y}\cdot\cot\theta\right)\right] \quad (3)$$

where E is the elastic modulus, σ_y is the yield strength, and θ is the half-angle of a conical indenter. It is possible to relate the conical indentation used for Eq. (3) to the triangular pyramidal indentation utilized in the current work by assuming that identical indentation responses are obtained when θ gives the same area-to-depth ratio as the pyramid, which gives the relation between ψ and θ as

$$\theta = \tan^{-1}\left(\sqrt{\frac{3\sqrt{3}}{\pi}}\cdot\tan\psi\right). \quad (4)$$

Thus, ψ = 35.3, 50, 65.3, 70, and 85° would correspond to θ = 42.3, 56.9, 70.3, 74.2, and 86.1°, respectively. With these θ values and E (~110 GPa for nt-Cu [1]; ~130 GPa for sc-Cu [29]) and σ_y (~0.6 GPa for nt-Cu [12]; ~0.068 GPa for sc-Cu [39]) obtained from literature, C_θ is estimated using Eq. (3). Only the case of ψ =85° for nt-Cu exhibits a low value of C_θ (~2.4) and all other cases show C_θ > 3. Thus, we consider C_θ = 3 (following Johnson [38]) except for the case of ψ =85° for nt-Cu. With these C_θ, $H_{O\text{-}P}$ is converted into $\sigma_{f,i}$. Note that we use $H_{O\text{-}P}$, instead of H_M, simply because we could not get proper SEM images for ψ =85°.

For the indentation or characteristic strain (ε_{char}) associated with each sharp indenter geometry, we employ Johnson [38]'s often used relationship

$$\varepsilon_{char} = 0.2\cdot\cot\theta \quad (5)$$

which is derived on the basis of an expanding cavity analogy. Note that a similar equation (with 0.22 as a multiplier instead of 0.2 in Eq. (5)) was also suggested by Sakai et al. [40] who conducted finite element analyses for elastic-perfectly-plastic and elastic-linear strain hardening

conical indentations. Eq. (5) leads to ε_{char} value for ψ = 85, 75, 65.3 (Berkovich), 50, and 35.3° (cube-corner) as 0.014, 0.042, 0.072, 0.13, and 0.22, respectively.

Variation of $\sigma_{f,i}$ with ε_{char} for both nt- and sc-Cu is plotted in Fig. 8. A substantial increase in $\sigma_{f,i}$ of nt-Cu, from ~0.5 GPa at ε_{char} = 0.014 to ~0.9 GPa at ε_{char} = 0.13 is noted, indicating that nt-Cu can strain harden in a substantial manner. Power-law fitting of the data in the ε_{char} range of 0.014-0.13 (i.e., ψ of 85-50°) yields the strain hardening exponent n (of $\sigma \propto \varepsilon^n$) of 0.23-0.27 (depending on indentation strain rate). Note that this n values are remarkably close to ~0.28 from tensile test in Fig. 1 of Ref. [1], which may imply that estimating stress-strain behavior by the method described here is meaningful.

As mentioned earlier, when the characteristic strains are increased further to 0.22 (i.e., ψ of 35.3°), the flow softening is seen. Mirshams and Pothapragada [41], who performed nanoindentation tests on nc-Ni with Berkovich and cube-corner indenters, report that $H_{O\text{-}P}$ obtained with the cube-corner indenter is much lower than that with Berkovich indenter. They speculated that this softening behavior for ψ = 35.3° might be related with some role of grain boundaries, but no detailed mechanisms were given.

For nt-Cu, earlier nanoindentation experiments using Berkovich tip [27] suggest that twin boundaries are much more stable than nc grains, which can grow under nanoindentation, leading to strong softening [42]. Although tensile tests of similar nt-Cu (Fig. 2 of Ref. [12]) also revealed a softening behavior after yielding, the softening observed at high strains in our work nonetheless remains quite intriguing as our nanoindentation direction is vertical to the twin boundaries (i.e., hard deformation mode) in which case strong strain hardening is normally expected [11,43] (that is consistent with the n values calculated above). To explore possible mechanisms of this softening behavior, we investigated the potential microstructure change

underneath the indenter for Berkovich (ψ =65.3^{o}) and cube-corner tips (ψ =35.3^{o}), as shown in the cross-sectional TEM images of Fig. 9. Observation of the deformation underneath indenter is important since deformation mechanism near the unconstrained surface play less important role during nanoindentation of nc materials than that underneath the indenter [44]. We note that the subsurface region underneath the hardness impression (Figs. 9a and 9b) exhibits quite different microstructures from that of undeformed region shown in Fig. 9c. Two features stand out in the figure. First, the collapse of twin structure occurred during the indentation (i.e., detwinning) in both indenters. Second, the collapsed region (i.e., detwinning area) for cube-corner indentation is much larger than that for Berkovich indentation, which may be due to the higher stresses and strains underneath sharper indenter. These results demonstrate that detwinning does occur underneath the indenter, likely caused by the intrinsically defective structures of twin boundaries, as suggested by recent TEM and in-situ synchrotron diffraction studies [45]. We hypothesize that the softening behavior for the cube-corner indentation is associated with this large amount of detwinning structures. In cube-corner indentation, large plastic strain produced underneath the indenter cannot be fully accommodated by surrounding nanotwin structures. As such, the material pile-up around hardness impression can be more pronounced. TEM image shown in Fig. 9d further indicates that no twin structure is observable in the pile-up region from the cube-corner indentation. These experimental results, although in contrast to some earlier reports [27], confirm that detwinning process can occur during the nanoindentation, which seems to become more severe at larger stresses and/or strains (i.e., using cube-corner indenter whose ε_{char} is 0.22). The localized detwinning processes observed here are nonetheless consistent with some other observations in the literature [46-48]. Note that the strains/stresses levels involved in our nanoindentation experiments and the grain boundary structure of our materials (which is

considered critically relevant to the detwinning process [45]) are substantially different from those reported in Ref. [27]. The nanoindentation induced microstructure change suggests that cautions need to be taken when one interprets the quantitative data acquired by different indenters (to be discussed in the next section).

Another possibility can be found in the previous MD simulation study of Shabib and Miller [49] who showed that after the strengthening effect reaches a maximum, large numbers of dislocations begin to cross the TBs and thus the stress starts to decrease. However, in this study, we could not find any experimental evidence for this scenario of dislocation transfer through TBs.

4.2 Strain-rate sensitivity, activation volume, and deformation mechanism

As mentioned earlier, m is an important material property, which enables an understanding of thermally-activated plastic deformation mechanisms, and is often determined at a given strain ε and temperature T by relating uniaxial flow stress σ_f and strain rate $\dot{\varepsilon}$ [50]:

$$m = \left(\frac{\partial \ln \sigma_f}{\partial \ln \dot{\varepsilon}} \right)_{\varepsilon,T} \quad . \tag{6}$$

For indentation, σ_f can be set as $\sigma_{f,i}$, whereas $\dot{\varepsilon}$ and the indentation strain rate, $\dot{\varepsilon}_i$ are related through the empirical relation $\dot{\varepsilon} \sim 0.01\dot{\varepsilon}_i$ [51]. Thus, m values at various ε_{char} have been estimated from the slopes of the double logarithmic plots of H/C_0 vs. $\dot{\varepsilon}_i$ displayed in Figs. 10a and 10b (for nt-Cu and sc-Cu, respectively). It is important to note here that the m measured from nanoindentations at different $\dot{\varepsilon}_i$ (as in this study) are often much smaller than those estimated from the nanoindentation creep data by simple conversion, $m = 1/n$ where n is creep stress exponent of $\dot{\varepsilon} = K(\sigma)^n$. However, the inverse relation between n and m may not be valid

because stress states utilized for determining n and m are substantially different from each other [52-54].

Variation of m with ε_{char} is displayed in Fig. 10c where the Berkovich indentation data (for sc-, cg-, and nc-Cu) obtained by Chen et al. [16] are also shown for comparison purposes. It is seen that the value of m estimated in the present work (~0.036) for nt-Cu and sc-Cu (0.006) are within the range reported in the literature (see Table 1 [1,7,10-12]). In Fig. 10c, the m values in Ref. [16] for nc-Cu (having d of ~40 nm), cg-Cu (d >100 μm), and (123) sc-Cu are in a good agreement with our results; i.e., the m for sc-Cu is similar to that found in the present study, and the cg-Cu is slightly higher than that for sc-Cu. It is noteworthy that nt-Cu with a twin spacing λ of 40 nm in this study has higher m than nc-Cu having similar d [16].

It is also evident in Fig. 10c that the m is sensitive to ε_{char}, with m reducing markedly from 0.07 to 0.25 as ε_{char} increases from 0.014 to 0.13. In the flow softening regime, i.e, $\varepsilon_{char} \geq$ 0.13, m remains invariant at ~0.025. In contrast, for sc-Cu, m essentially remains invariant – and mostly very low (< ~0.01) – throughout the range of ε_{char} examined in this work. The dependency of m on ε_{char} in nt-Cu is not surprising though, as SRS is known to be a function of deformation strains in face-centered cubic nanostructured metals [55]. However, the magnitude of variation (a factor of more than 3) obtained by various indenters here is surprising, suggesting the critical importance of selecting proper indenters and indentation conditions when reporting m for various nanostructured materials. In a relevant study, the strain-dependency of the m in a nt-Cu sample (having average twin lamellar spacing of 15 ± 7 nm) was reported by Shen et al. [10] who evaluated the change in m with strain rate and plastic strain through tensile strain rate jump tests. It was found that the m slightly decreases with strain from ~0.046 ± 0.006 at $\varepsilon \sim 0.012$ to ~0.034 ± 0.006 at $\varepsilon \sim 0.03$ [10]. While the examined strain range in Ref. [10] is limited (0.01-

0.03), the strain dependency of the m is in good agreement with our data for ε_{char} ranging from 0.014 to 0.072. Shen et al. [10] attribute this behavior to the deformation-induced twin spacing increase. In a separate study using nanoindentation, Ye et al. [11] discovered an increased m in polished nt-Cu sample (γ~40 nm) that contains higher dislocation density, suggesting that m is generally enhanced with strain if twin spacing is unmodified. Our results in Fig. 10 suggest a decreasing m with increasing strains. However, as discussed above, detwinning occurs in the samples when using small ψ indenters (< 65.3°); i.e., the measured m values under small ψ may not be representative of the initial microstructure. On the other hand, due to the contact area measurement uncertainty of large angle indenter (85°), the obtained rather high m from this indenter should also be disregarded. Instead, two m values obtained at ψ =75° and ψ =65.3° seem to be the most representative values of this material, in consistent with those reported in Ref. [11].

With m, the activation volume V^*, which is defined as

$$V^* = \sqrt{3}kT\left(\frac{\partial \ln \dot{\varepsilon}}{\partial \sigma_f}\right) = C_\theta \sqrt{3}kT\left(\frac{\partial \ln \dot{\varepsilon}}{\partial H}\right) \tag{7}$$

where k is the Boltzmann constant and T is the absolute temperature, also provides an useful clue for the plastic deformation mechanism of metals since it can vary by orders of magnitude for different rate-limiting processes [56]. Typical magnitude of V^* for the forest dislocations cutting mechanism in single crystal or cg metals (especially, having fcc structure) is of the order of several hundred to a couple of thousand time b^3 [57]. In nc metals, the V^* for dislocation-mediated flow is known to be reduced to the order of several ten times b^3 since dislocation nucleation sources are changing from typical Frank-Read source to grain boundaries [8,58]. In this case, the plastic flow is accommodated by the interaction of dislocations with various boundaries such as grain boundaries. In nt metals, slip behavior are mediated by TBs, and thus reduced V^* is observed according to small average λ (even in nt metals having d of several

hundred nanometer [56]). According to Eq. (7), the V^* values of nt-Cu could be estimated from the slope of the linear fit of logarithmic strain rate versus linear flow stress in Fig. 11a. The results are summarized in Fig. 11b where with increasing indenter angle the V^* of the nt-Cu increases mildly with reducing ψ (from ~$12b^3$ for $\psi = 85°$ to ~$20b^3$ for $\psi = 35.3°$). The V^* for the sc-Cu (not shown here) is in the range of ~200-$500b^3$ (which in agreement with literature data [16]) and does not exhibit meaningful change with ψ as one might expect from the angle-independent m values.

The estimated V^* values clearly show a small variation trend than m, and may have suggested that the main deformation mechanism for different indenters remains in the regime of TBs-mediated dislocation flow. This qualitative picture however cannot accurately describe the rather complex microstructure evolutions observed in our TEM experiments, suggesting that the V^* alone is insufficient to infer the complete deformation mechanisms. The slightly larger V^* under smaller ψ is not surprising, considering far more coarsened post-indentation microstructure (i.e., detwinning) for smaller ψ.

From the nanoindentation technique point of view, an important question that is unresolved yet is "how does the angle variation induce the trends of V^* and m?" One possibility (although its detailed mechanism is not fully understood) may be associated with the volume of the plastic-zone underneath the indenter. According to Johnson's expanding cavity model for a conical indentation, the volume can be given as:

$$V_{\text{ind}} = \frac{2\pi r_{\text{p}}^3}{3} = \frac{2\pi a_{\text{c}}^3}{18(1-\nu)}\left[\frac{E}{\sigma_{\text{y}}}\tan\left(\frac{\pi}{2}-\theta\right)+4(1-2\nu)\right] \tag{8}$$

where r_p is the radius of plastic zone, a_c is the contact radius and v is the Poison's ratio [59]. This equation suggests that, for a given indentation load, the volume of the transformed zone will

increase with increasing sharpness (or reducing angle), as shown in Fig. 12. Although there is no clue for correlating V_{ind} and V^*, similar trends are found in both volumes; i.e., each volume increases with decreasing ψ, and sc-Cu has much larger volume than nt-Cu. This may imply a possibility that, if it is assumed that indentation-induced plastic strain is accumulated by the similar number of thermally-activated events, the probability of the occurrence of larger-V^*-based events can be higher for larger V_{ind}. Again, however, this scenario is not fully understood at this point and needs further investigation.

6. Conclusions

Nanoindentation is a common technique to explore the mechanical properties of nanostructured metals (nanocrystalline, nanotwinned, and ultrafine-grained materials) due to the simplicity of the method and a relatively small amount of materials required. However, the influence of various indentation parameters on the measured mechanical properties is little known. Using nt-Cu as a model system, we have investigated the contact angle influence on the hardness, strain-rate sensitivity, and activation volume of nt-Cu (λ~40-80 nm). Through a series of nanoindentation tests using five different indenters having different indenter angle and comparing the results with those of sc-Cu, we find that the set of deformation parameters of nt-Cu depends sensitively upon the indenter types, in contrast to those of sc-Cu. At the smallest indenter angle (cube-corner indenter, ψ =35.3°), which corresponds to the highest strains (~0.22), we observe flow softening behavior, a lowest strain rate sensitivity (~0.024), and the largest activation volume (~$20b^3$). TEM investigations reveal detwinning and grain coarsening behavior under these nanoindentation conditions. On the other hand, a high strain rate sensitivity (~0.07) and small activation volume (~$12b^3$) are observed for ψ =85°, complicated by the uncertainties of

contact area measurements. We discuss the limitations and implications of these physical parameters on the deformation mechanisms of nt-Cu.

Acknowledgements

This research was supported by Basic Science Research Program through the National Research Foundation of Korea (NRF) funded by the Ministry of Education, Science and Technology (No. 2010-0025526), and in part by the Human Resources Development of the Korea Institute of Energy Technology Evaluation and Planning (KETEP) grant funded by the Korea government Ministry of Knowledge Economy (No. 20114010203020). The work at LLNL was performed under the auspices of the US Department of Energy by Lawrence Livermore National Laboratory under Contract No. DE-AC52-07NA27344.

References

1. Dao M, Lu L, Shen YF, Suresh S. Acta Mater 2006;54:5421.
2. Lu K, Lu L, Suresh S. Science 2009;324:349.
3. Kumar KS, Swygenhoven HV, Suresh S. Acta Mater 2003;51:5743.
4. Lu L, Chen X, Huang X, Lu K. Science 2009;323:607.
5. Zhang X, Misra A. Scripta Mater 2012;66:860.
6. Lu L, Shen Y, Chen X, Qian L, Lu K. Science 2004;304:422.
7. Lu L, Schwaiger R, Shan ZW, Dao M, Lu K, Suresh S. Acta Mater 2005;53:2169.
8. Wang YM, Hamza AV, Ma E. Acta Mater 2006;54:2715.
9. Asaro RJ, Suresh S. Acta Mater 2005;53:3369.
10. Shen YF, Lu L, Dao M, Suresh S. Scripta Mater 2006;55:319.
11. Ye JC, Wang YM, Barbee TW, Hamza AV. Appl Phys Lett 2012;100:261912.
12. Hodge AM, Wang YM, Barbee Jr TW. Scripta Mater 2008;59:163.
13. Carreker RP, Hibbard WR. Acta Metall 1953;1:656.
14. Follansbe PS, Kocks UF. Acta Metall 1988;36:81.
15. Shen YF, Lu L, Lu QH, Jin ZH, Lu K. Scripta Mater 2005;52:989.
16. Chen J, Lu L, Lu K. Scripta Mater 2006; 54: 1913.
17. Trelewicz JR, Schuh CA. Acta Mater 2007;55:5948.
18. Schwaiger R, Moser B, Dao M, Chollacoop N, Suresh S. Acta Mater 2003;51:5159.
19. Maier V, Durst K, Mueller J, Backes B, Höppel W, Göken M. J Mater Res 2011;26:1421

20. Choi I-C, Yoo B-G, Kim Y-J, Seok M-Y, Wang YM, Jang J-i. Scripta Mater 2011;65:300.
21. Jang J-i, Lance MJ, Wen S, Tsui TY, Pharr GM. Acta Mater 2005;53:1759.
22. Jang J-i, Pharr GM. Acta Mater 2008;56:4458.
23. Shim S, Jang J-i, Pharr GM. Acta Mater 2008;56:3824.
24. Jang J-i, Yoo B-G, Kim Y-J, Oh J-H, Choi I-C, Bei H. Scripta Mater 2011;64:753.
25. Lucas BN, Oliver WC. Metall Mater Trans A 1999;30A:601.
26. Oliver WC, Pharr GM. J Mater Res 1992;7:1564.
27. Bezares J, Jiao S, Liu Y, Bufford D, Lu L, Zhang X, Kulkarni Y, Asaro RJ. Acta Mater 2012;60:4623.
28. Anderoglu O, Misra A, Ronning F, Wang H, Zhang X. J Appl Phys 2009;106:024313.
29. Vlassak JJ, Nix WD. J Mech Phys Solids 1994;42:1223.
30. Oliver WC, Pharr GM. J Mater Res 2004;19:3.
31. Strader JH, Shim S, Bei H, Oliver WC, Pharr GM. Philos Mag 2006;86:5285.
32. Bolshakov A, Pharr GM. J Mater Res 1998;13:1049.
33. Lee YH, Hahn JH, Nahm SH, Jang JI, Kwon D. J Phys D: Appl Phys 2008;41:074027.
34. Yoo BG, Park KW, Lee JC, Ramamurty U, Jang JI. J Mater Res 2009;24:1405.
35. Tabor D. The hardness of metals. Oxford: Oxford University Press; 1951.
36. Atkins AG, Tabor D. J Mech Phys Solids 1970;18:115.
37. Wang YM, Ott RT, van Buuren T, Willey TM, Biener MM, Hamza AV. Phys Rev B 2012;85:014101.
38. Johnson KL. Contact mechanics. Cambridge: Cambridge University Press; 1985.
39. Hertzberg RW. Deformation and Fracture Mechanics of Engineering Materials. New York: John Wiley & Sons; 1989.
40. Sakai M, Akatsu T, Numata S, Matsuda K. J Mater Res 2003;18:2087.
41. Mirshams RA, Pothapragada RM. Acta Mater 206;54:1123.
42. Zhang K, Weertman JR, Eastman JA. Appl Phys Lett 2005;87:061921.
43. You Z, Li X, Gui L, Lu Q, Zhu T, Gao H, Lu L. Acta Mater 2013;61:217.
44. Maier V, Merle B, Göken M, Durst K. J Mater Res 2013;28:1177.
45. Wang YM, Sansoz F, LaGrange T, Ott RT, Marian J, Barbee Jr TW, Hamza AV. Nature Mater. advance online publication, 19 May 2013 (doi: 10.1038/nmat3646)
46. Hodge AM, Furnish TA, Shute CJ, Liao Y, Huang X, Hong CS, Zhu YT, Barbee Jr TW, Weertman JR. Scripta Mater 2012;66:872.
47. Shute CJ, Myers BD, Xie S, Li S-Y, Barbee Jr TW, Hodge AM, Weertman JR. Acta Mater 2011;59:4569.
48. Yu KY, Bufford D, Sun C, Liu Y, Wang H, Kirk MA, Li M, Zhang X. Nature Comm 2013; 4:1377.
49. Shabib I, Miller RE. Acta Mater 2009;57:4364.
50. Mayo MJ, Nix WD. Acta Metall 1988;36:2183.
51. Wang CL, Lai YH, Huang JC, Nieh TG. Scripta Mater 2010;62:175.
52. Choi I-C, Yoo B-G, Kim Y-J, Jang J-i. J Mater Res 2012;27:3.
53. Yoo B-G, Kim J-Y, Kim Y-J, Choi I-C, Shim S, Tsui TY, Bei H, Ramamurty U, Jang J-i. Int J Plasticity 2012;37:108.
54. Choi I-C, Kim Y-J, Seok M-Y, Yoo B-G, Kim J-Y, Wang Y, Jang J-i. Int J Plasticity 2013; 41: 53.
55. Wang YM, Ma E. Acta Mater 2004;52:1699.

56. Zhu T, Li J, Samanta A, Kim HG, Suresh S. P Natl Acad Sci USA 2007;104:3031.
57. Conrad H. Mater Sci Eng A 2003;341:216.
58. Ma E. Science 2004;305:623.
59. Johnson KL. J Mech Phys Solids 1970;18:115.

List of Tables and Figures

Table 1

λ [nm]	d [nm]	Testing method	Strain rate [s^{-1}]	m	V^* [b^3]	Ref.
~15	~400	T	~10^{-4}-10^{-1}	0.037±0.014		[1]
~15	400-500	J	~10^{-5}-10^{-2}	0.035-0.046		[10]
~20	~500	I	0.1-100 mN/s	0.036±0.009	~12	[7]
~35	~450	T	~10^{-4}-10^{-1}	0.026±0.012		[1]
~40	~3000	I	~10^{-4}-10^{-2}	0.047±0.003	16.1±2.0	[11]
40-80	500-600	T	~10^{-5}-10^{-2}	0.021		[12]
~90	~500	I	0.1-100 mN/s	0.025±0.009	~22	[7]
~100	400-500	J	~10^{-5}-10^{-2}	0.015-0.020		[10]
~100	~425	T	~10^{-4}-10^{-1}	0.012±0.010		[1]

Table 2

		35.3°	**50°**	**65.3°**	**75°**
nt-Cu	A **[μm^2]**	42.81±0.54	41.13±0.84	48.54±1.72	55.70±2.50
sc-Cu	A **[μm^2]**	124.7±1.17	149.39±2.15	179.37±3.19	225.53±7.75

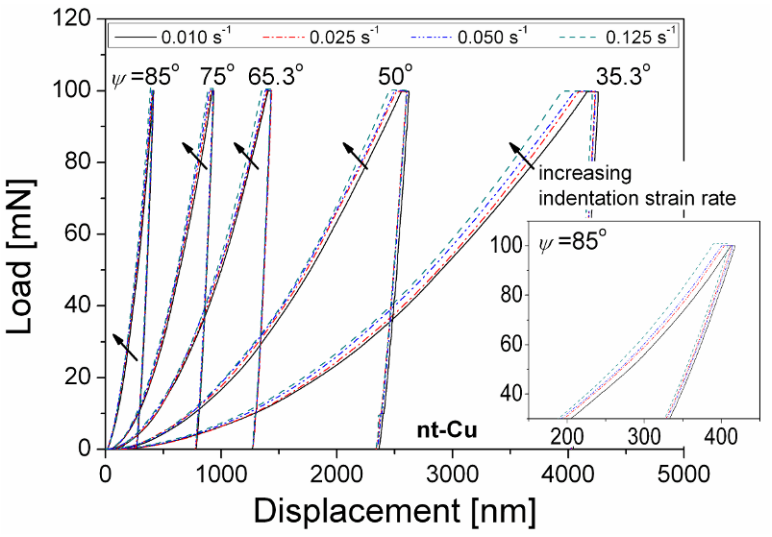
0.010 s-1
0.025 s-1
0.050 s-1
0.125 s-1
ψ =85°
75°
65.3°
50°
35.3°
increasing
indentation strain rate
ψ =85°
nt-Cu
Load [mN]
Displacement [nm]

(a)

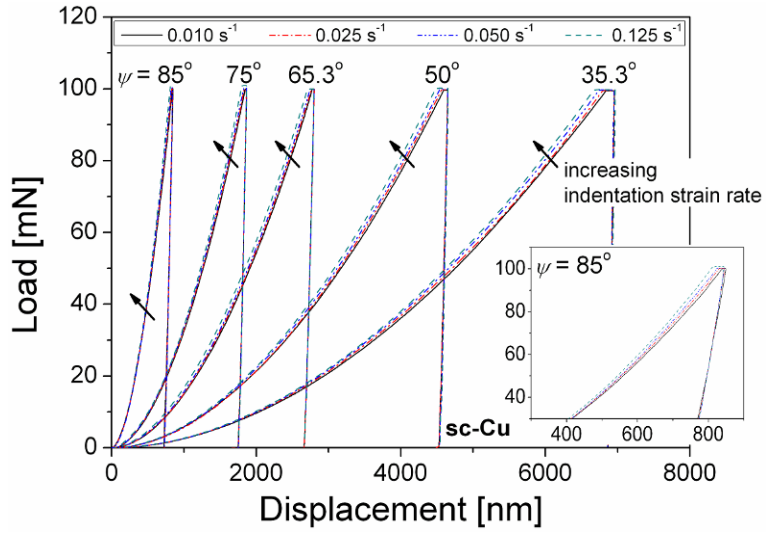
0.010 s-1
0.025 s-1
0.050 s-1
0.125 s-1
ψ = 85°
75°
65.3°
50°
35.3°
increasing
indentation strain rate
ψ = 85°
sc-Cu
Load [mN]
Displacement [nm]

(b)

Fig. 1

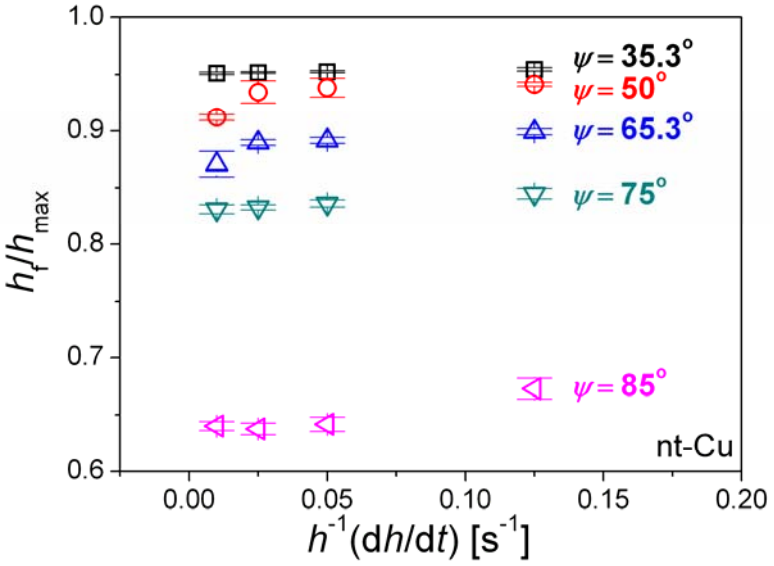
1.0
0.9
0.8
0.7
0.6
h_f/h_{max}
0.00
0.05
0.10
0.15
0.20
$h^{-1}(dh/dt)$ [s^{-1}]
$\psi = 35.3°$
$\psi = 50°$
$\psi = 65.3°$
$\psi = 75°$
$\psi = 85°$
nt-Cu

(a)

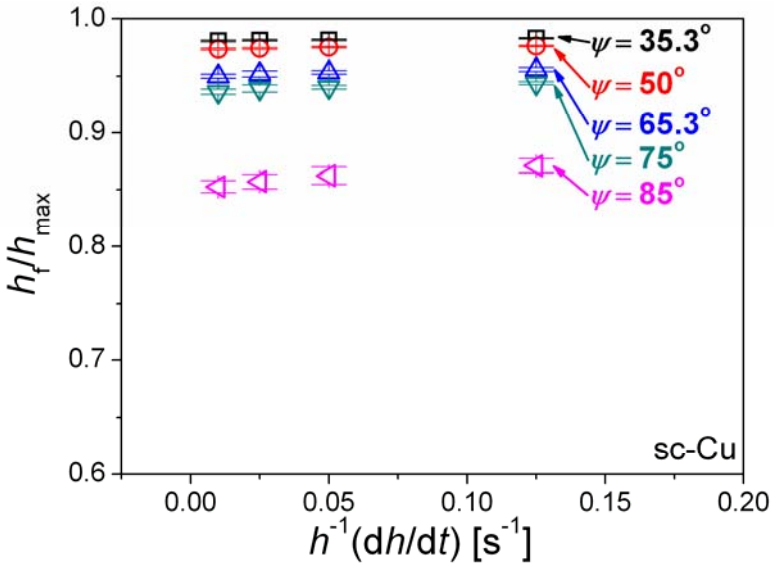
1.0
0.9
0.8
0.7
0.6
h_f/h_{max}
0.00
0.05
0.10
0.15
0.20
$h^{-1}(dh/dt)$ [s^{-1}]
$\psi = 35.3°$
$\psi = 50°$
$\psi = 65.3°$
$\psi = 75°$
$\psi = 85°$
sc-Cu

(b)

Fig. 2

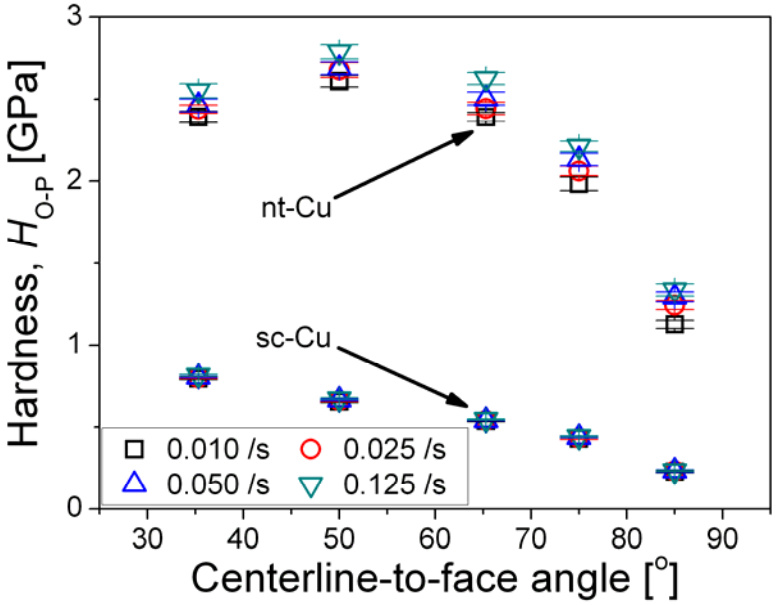
Hardness, H_{O-P} [GPa]
Centerline-to-face angle [°]
nt-Cu
sc-Cu
0.010 /s
0.025 /s
0.050 /s
0.125 /s
0
1
2
3
30
40
50
60
70
80
90

Fig. 3

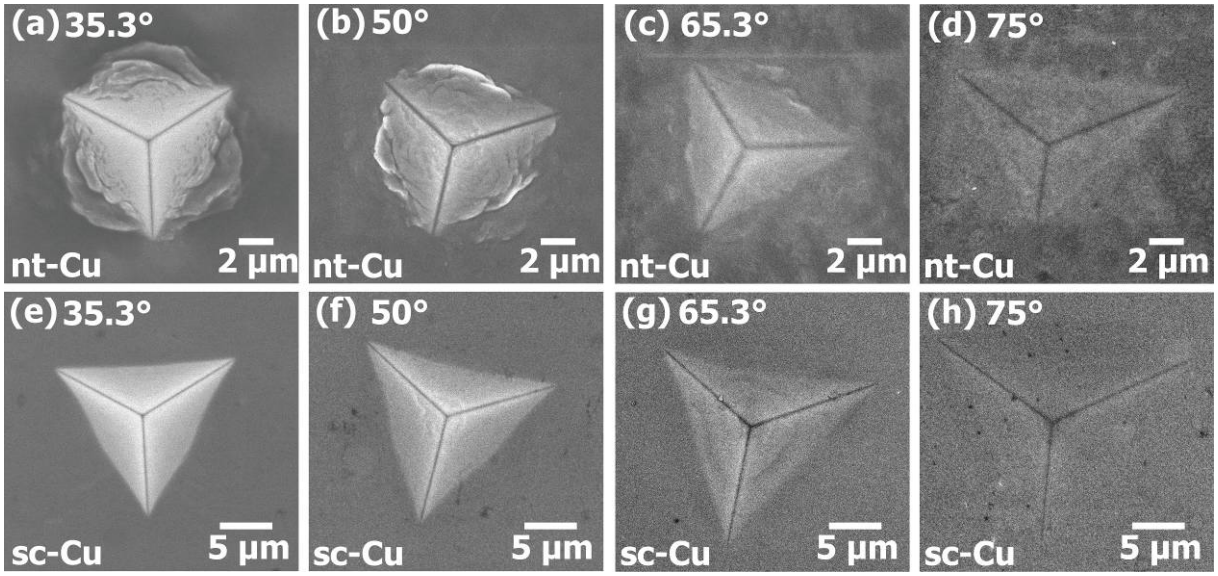
(a) 35.3°
nt-Cu
2 μm
(b) 50°
nt-Cu
2 μm
(c) 65.3°
nt-Cu
2 μm
(d) 75°
nt-Cu
2 μm
(e) 35.3°
sc-Cu
5 μm
(f) 50°
sc-Cu
5 μm
(g) 65.3°
sc-Cu
5 μm
(h) 75°
sc-Cu
5 μm

Fig. 4

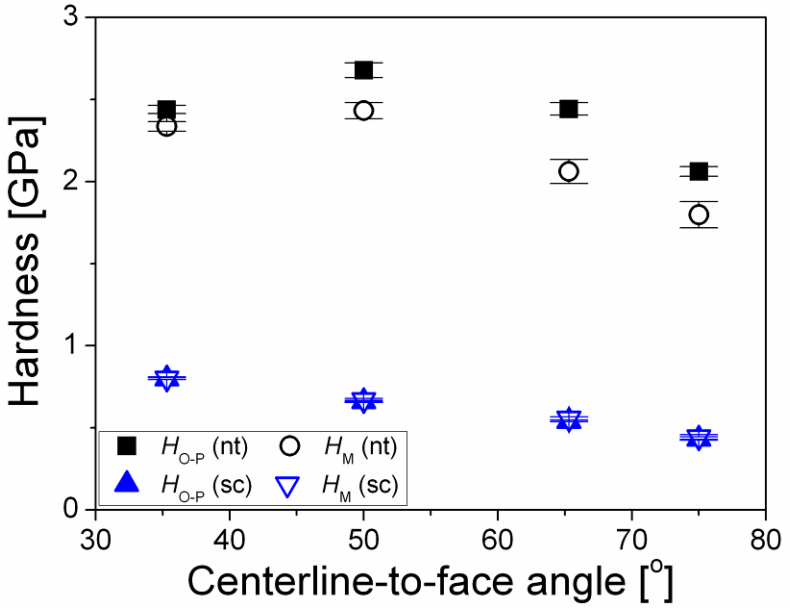
Hardness [GPa]
Centerline-to-face angle [°]
0
1
2
3
30
40
50
60
70
80
H_O-P (nt)
H_M (nt)
H_O-P (sc)
H_M (sc)

Fig. 5

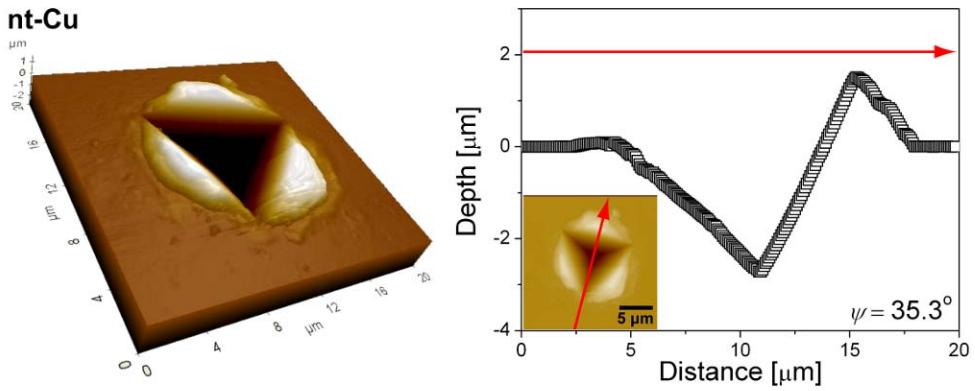
nt-Cu
Depth [μm]
Distance [μm]
5 μm
ψ = 35.3°

(a)

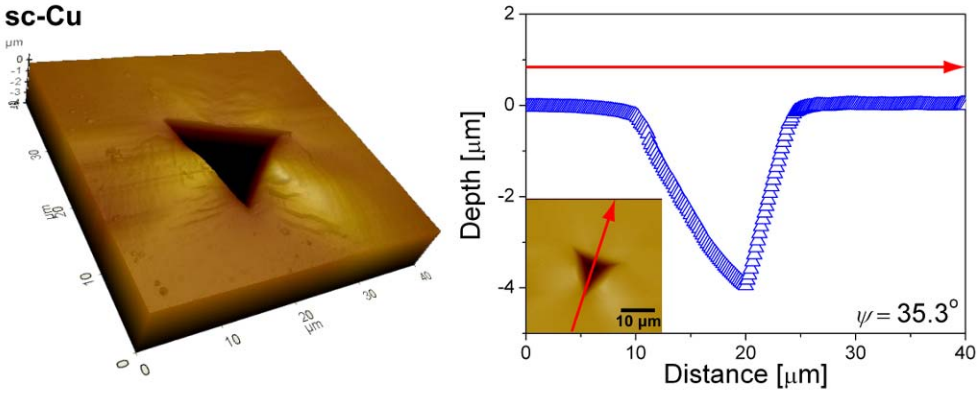
sc-Cu
Depth [μm]
Distance [μm]
10 μm
ψ = 35.3°

(b)

Fig. 6

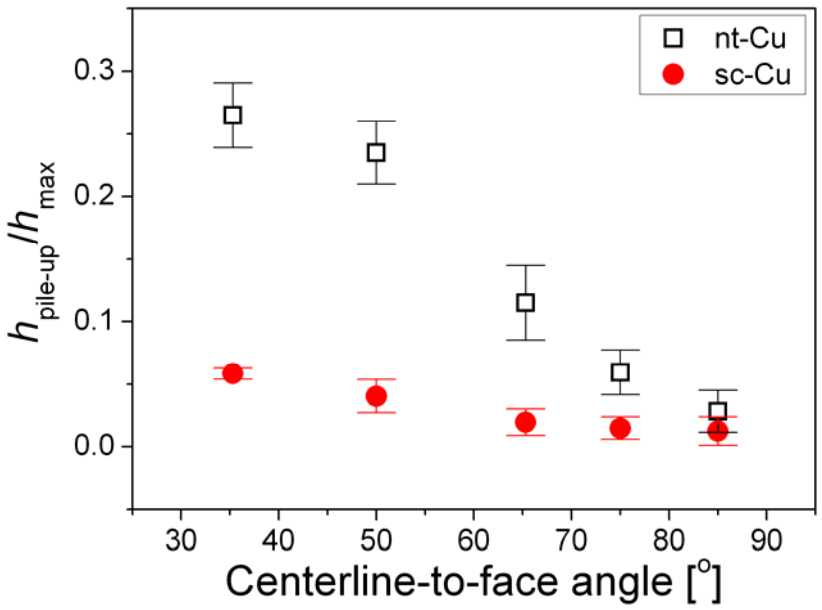
nt-Cu
sc-Cu
0.3
0.2
0.1
0.0
$h_{pile\text{-}up}/h_{max}$
30
40
50
60
70
80
90
Centerline-to-face angle [°]

Fig. 7

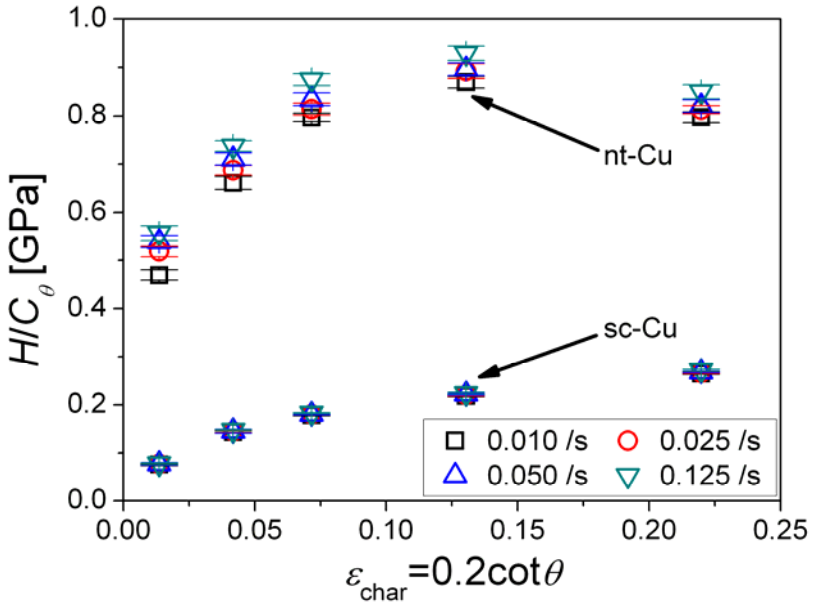
1.0
0.8
0.6
0.4
0.2
0.0
H/C_θ [GPa]
0.00
0.05
0.10
0.15
0.20
0.25
ε_char=0.2cotθ
nt-Cu
sc-Cu
0.010 /s
0.025 /s
0.050 /s
0.125 /s

Fig. 8

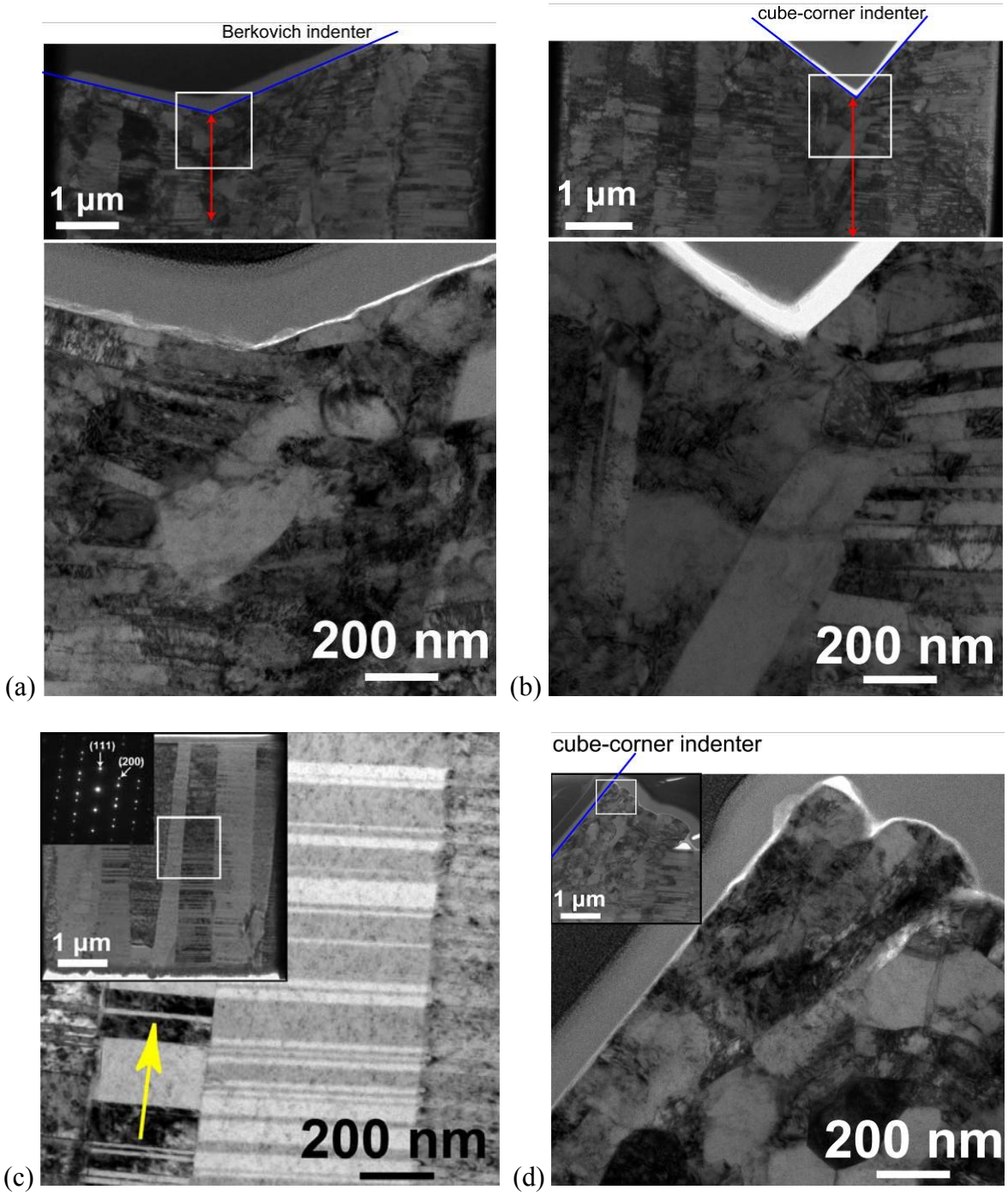
Berkovich indenter
1 μm
200 nm
(a)
cube-corner indenter
1 μm
200 nm
(b)
(111)
(200)
1 μm
200 nm
(c)
cube-corner indenter
1 μm
200 nm
(d)

Fig. 9

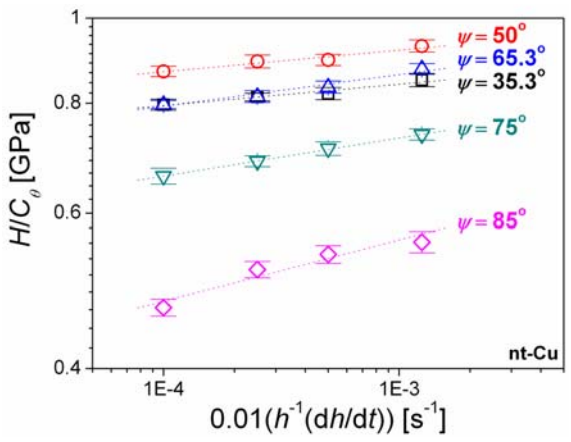
1
0.8
0.6
0.4
H/C_θ [GPa]
$\psi = 50°$
$\psi = 65.3°$
$\psi = 35.3°$
$\psi = 75°$
$\psi = 85°$
nt-Cu
1E-4
1E-3
$0.01(h^{-1}(dh/dt))$ [s^{-1}]

(a)

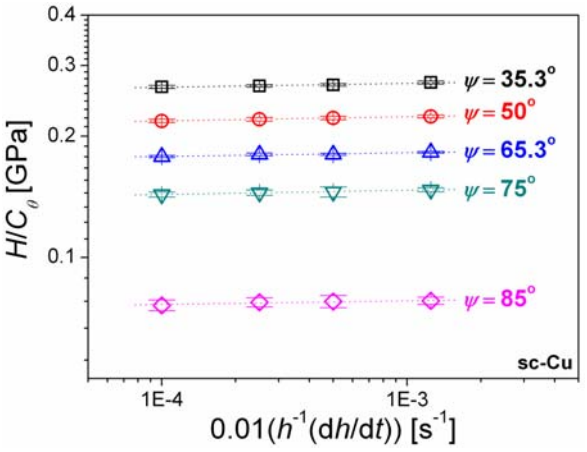
0.4
0.3
0.2
0.1
H/C_θ [GPa]
$\psi = 35.3°$
$\psi = 50°$
$\psi = 65.3°$
$\psi = 75°$
$\psi = 85°$
sc-Cu
1E-4
1E-3
$0.01(h^{-1}(dh/dt))$ [s^{-1}]

(b)

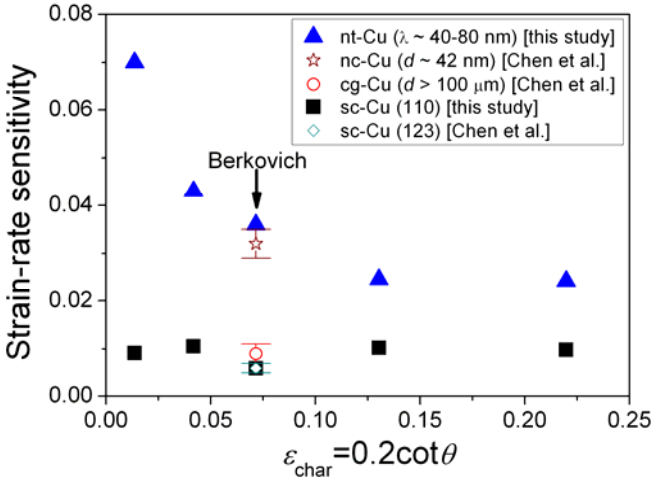
0.08
0.06
0.04
0.02
0.00
Strain-rate sensitivity
nt-Cu (λ ~ 40-80 nm) [this study]
nc-Cu (d ~ 42 nm) [Chen et al.]
cg-Cu (d > 100 μm) [Chen et al.]
sc-Cu (110) [this study]
sc-Cu (123) [Chen et al.]
Berkovich
0.00
0.05
0.10
0.15
0.20
0.25
ε_{char}=0.2cotθ

(c)

Fig. 10

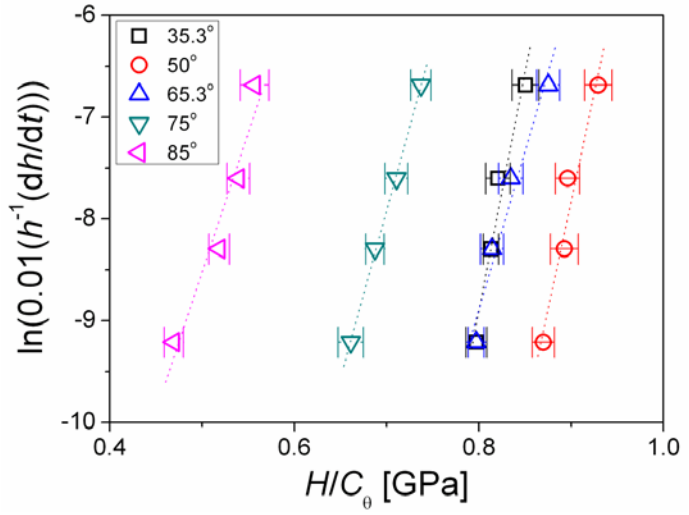
35.3°
50°
65.3°
75°
85°
ln(0.01(h^-1(dh/dt)))
H/C_θ [GPa]
-6
-7
-8
-9
-10
0.4
0.6
0.8
1.0

(a)

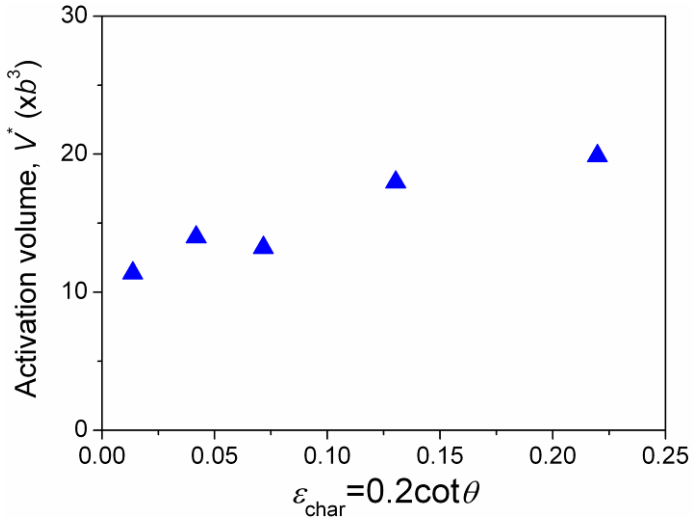
Activation volume, V* (xb^3)
ε_char=0.2cotθ
30
20
10
0
0.00
0.05
0.10
0.15
0.20
0.25

(b)

Fig. 11

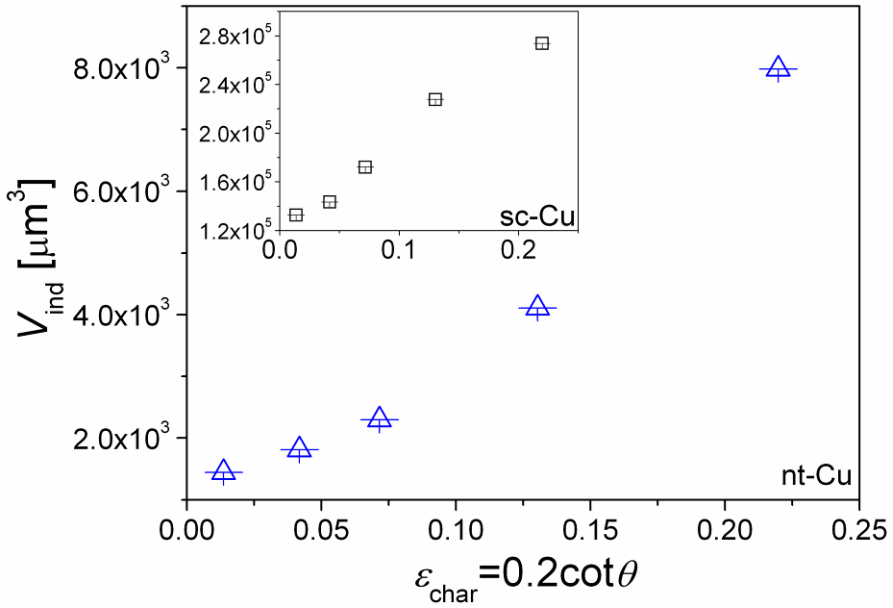
8.0x10^3
6.0x10^3
4.0x10^3
2.0x10^3
V_ind [μm^3]
0.00
0.05
0.10
0.15
0.20
0.25
ε_char=0.2cotθ
nt-Cu
2.8x10^5
2.4x10^5
2.0x10^5
1.6x10^5
1.2x10^5
0.0
0.1
0.2
sc-Cu

Fig. 12